ACS APPLIED MATERIALS & INTERFACES

Research Article

Cite This: ACS Appl. Mater. Interfaces 2017, 9, 36745-36754

www.acsami.org

Enhancing the Ion Transport in $LiMn_{1.5}Ni_{0.5}O_4$ by Altering the Particle Wulff Shape via Anisotropic Surface Segregation

Jiajia Huang,[†] Haodong Liu,[†] Naixie Zhou,[†] Ke An,[‡] Ying Shirley Meng,[†] and Jian Luo*[,†]

[†]Department of NanoEngineering, Program of Materials Science and Engineering, University of California, San Diego, 9500 Gilman Drive, La Jolla, California 92093-0448, United States

[‡]Chemical and Engineering Materials Division, Oak Ridge National Laboratory, Oak Ridge, Tennessee 37830, United States

ABSTRACT: Spontaneous and anisotropic surface segregation of W cations in $LiMn_{1.5}Ni_{0.5}O_4$ particles can alter the Wulff shape and improve surface stability, thereby significantly improving the electrochemical performance. An Auger electron nanoprobe was employed to identify the anisotropic surface segregation, whereby W cations prefer to segregate to {110} surface facets to decrease its relative surface energy according to Gibbs adsorption theory and subsequently increase its surface area according to Wulff theory. Consequently, the rate performance is improved (e.g., by ~5-fold at a high rate of 25C) because the {110} facets have more open channels for fast lithium ion diffusion. Furthermore, X-ray photoelectron spectroscopy (XPS) depth profiling suggested that the surface segregation and partial reduction of W cation inhibit the formation of Mn^{3+} on surfaces to improve cycling stability via enhancing the cathode electrolyte interphase (CEI) stability at high charging voltages. This is the first report of using anisotropic surface segregation to thermodynamically control the particle morphology as well as enhancing CEI stability as a facile, and potentially general, method to significantly improve the electrochemical performance of battery electrodes. Combining neutron diffraction, an Auger electron nanoprobe, XPS, and other characterizations, we depict the underlying mechanisms of improved ionic transport and CEI stability in high-voltage $LiMn_{1.5}Ni_{0.5}O_4$ spinel materials.

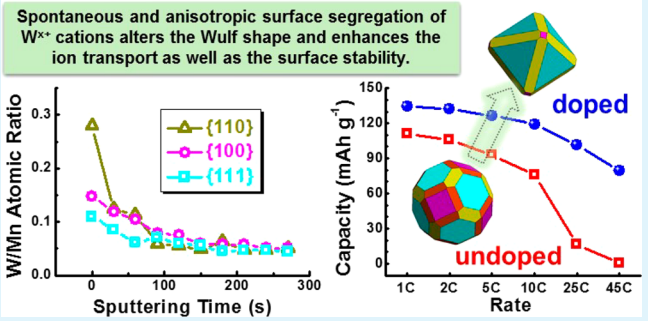

KEYWORDS: *lithium-ion batteries, high-voltage spinel, anisotropic surface segregation, Wulff shape, neutron diffraction*

1. INTRODUCTION

High-voltage $LiMn_{1.5}Ni_{0.5}O_4$ spinel is one of the most promising candidates for next-generation cathode materials of lithium ion batteries for electric vehicles and other high-energy density applications due to its high operating voltage ~4.7 V, low cost, and environmental friendliness. Prior studies had investigated the effects of Mn and Ni cation disordering,[1−5] Mn^{3+} concentration,[2,6,7] oxygen vacancies,[1,8,9] impurities,[4,10] surface coating,[11,12] cation doping,[5,13−18] and particle surface crystalline orientation[19−27] on improving the electrochemical performance. Several reviews on high-voltage spinel cathodes have been published recently.[28−35] However, the roles of cation doping on surface segregation and the particle morphology, as well as their subsequent impacts on the electrochemical performance, have not been well established in general.

Several recent studies suggested that the crystalline orientations on the particle surfaces can have significant influences on the electrochemical properties.[19−27] In most experiments, different crystalline facets were found to coexist at the surfaces of $LiMn_{1.5}Ni_{0.5}O_4$ particles:[21−27] {111} and {100} surface facets were most frequently observed. Thermodynamically, {111} and {100} facets tend to coexist due to their similar (low) surface energies, while eliminating {100} facets appears to benefit rate capability and cycling stability.[22] Chemelewski et al. synthesized $LiMn_{1.5}Ni_{0.5}O_4$ particles with dominating {111} surface facets by an improved coprecipitation method to kinetically control the particle morphology to eliminate {100} facets, which achieved an improved rate performance comparing to that of particles with coexisting {100} surface facets synthesized by a traditional coprecipitation method.[22] Interestingly, it also showed that Fe doping could promote the formation of {111} surface facets of $LiMn_{1.5}Ni_{0.5}O_4$ particles, though its underlying mechanism remained unclear.

Besides {111} and {100} surface facets, a smaller fraction of {110} facets was also observed occasionally.[24] The {110} facets exhibit the most open channels for fast lithium diffusion but appear to have a higher surface energy, which is not thermodynamically favorable to form compared to {111} and {100}.[36] Here, we have demonstrated a novel strategy to increase the fraction of the most favorite {110} facets thermodynamically to improve the rate capabilities via anisotropic surface segregation of WO_3, along with enhancing the cycling stability via improving the surface stability. Moreover, we have conducted a combination of neutron

Received: July 8, 2017
Accepted: October 3, 2017
Published: October 3, 2017

DOI: 10.1021/acsami.7b09903
ACS Appl. Mater. Interfaces 2017, 9, 36745−36754

diffraction, X-ray photoelectron spectroscopy (XPS), an Auger electron nanoprobe, and other characterizations to verify our hypothesis and reveal the underlying mechanisms at multiple length scales.

Furthermore, prior reports already suggested that the surface segregation of dopants can influence the electrochemical performance of $LiMn_{1.5}Ni_{0.5}O_4$.[5,37,38] Though surface segregation appears to be related to the particle morphology change,[38] the relation between the two phenomena has not been investigated. (In fact, it was often believed that particle morphology was mostly determined by kinetics and the influence surface segregation is unimportant.)[30] Here, we demonstrate, to our knowledge for the first time, that the anisotropic segregation of W cation preferably on the {110} surface facets of $LiMn_{1.5}Ni_{0.5}O_4$ can stabilize the most favorite {110} facets with the most open channels for fast lithium diffusion, in accord with the well-established Gibbs and Wulff theories. Consequently, the surface segregation and associated particle morphological changes contribute to significant improvements of both rate capabilities and cycling stabilities of the high-voltage $LiMn_{1.5}Ni_{0.5}O_4$ cathode.

It should be noted that aliovalent doping can also change the Mn^{3+} concentration, which can influence the formation of oxygen vacancies and cation disordering (both inside the bulk phase and at/near the surface). The existence of Mn^{3+} cations benefits the rate capability by increasing both of the lithium ion bulk diffusion rate and the electronic conductivity, and it contributes an extra amount of discharge capacity from Mn^{3+}/Mn^{4+} redox at the voltage plateau of ~4 V.[2,6] In contrast, the presence of Mn^{3+} cations decreases cycling stability by promoting the formation of Mn^{2+} on surface and subsequently dissolution of Mn^{2+} in the electrolyte.[15,39] Notably, a prior study also demonstrated that surface segregation of Fe, Cr and Ga in $LiMn_{1.5}Ni_{0.5}O_4$ particles could inhibit the Mn^{2+} dissolution in electrolyte to subsequently improve the cycling stability.[5] In this study, we further demonstrated via XPS depth profiling that the surface segregation and partial reduction of W cation inhibit the formation of Mn^{3+} on surfaces to improve cycling stability presumably via enhancing the cathode electrolyte interphase (CEI) at high charging voltages.

In this study, we added 1 vol % WO_3, which is a well-known "supported oxide catalyst" that would spontaneously spread (adsorb) on the surfaces of inert oxides (typically Al_2O_3 and TiO_2 nanoparticles) upon annealing due to its low surface energy,[40−42] to $LiMn_{1.5}Ni_{0.5}O_4$, which representing a facile and cost-effective "mixing and annealing" process. We further demonstrated that WO_3 dissolved into the $LiMn_{1.5}Ni_{0.5}O_4$ bulk phase and anisotropically adsorbed (a.k.a. segregated) on the surfaces of $LiMn_{1.5}Ni_{0.5}O_4$ particles to increase the fraction of the most favorite {110} facets.[24] The combination effects of bulk doping, surface segregation, and anisotropic-segregation-induced morphological changes improved not only rate capabilities substantially (e.g., an ~500% increase in the discharge capacity at 25C) but also the cycling stability (e.g., > 25% increase in the discharge capacity at 55 °C after 200 cycles at 1C).

2. EXPERIMENTAL SECTION

To prepare 1 vol % WO_3-doped $LiMn_{1.5}Ni_{0.5}O_4$ (a nominal volumetric percentage calculated using the molar volumes of individual compounds, corresponding to an overall W/Mn atomic ratio of ~0.06), $(NH_4)_2WO_4$ (precursor for WO_3) was added to as-received $LiMn_{1.5}Ni_{0.5}O_4$ (Sigma-Aldrich, > 99%) and dispersed in 4 mL of acetone. The mixture was placed in a silicon nitride grinding vial with two silicon nitride balls. Before sealing the jar, the corprene gasket was taped by Teflon to protect it from acetone corrosion and precursor contamination. High-energy ball-milling was carried out using a SPEX 8000D mill for a duration of 10 min, followed by a 15 min resting interval; this milling process was repeated 3 times. The mixture was dried isothermally in an oven around 70 °C. The dried powder was placed in a covered alumina crucible, isothermally annealed at 800 °C for 4 h in a box furnace with a heating rate of 5 °C/min, and subsequently cooled in the furnace (with power being shut down) after the isothermal annealing. As a reference, controlled specimens of undoped $LiMn_{1.5}Ni_{0.5}O_4$ were prepared with exactly the same ball-milling and annealing procedure as that described above but without the addition of the WO_3 precursor ($(NH_4)_2WO_4$).

Particle sizes and morphologies were characterized using a FEI XL30 scanning electron microscope (SEM). Specific surface area was measured on a Micromeritics ASAP-2000 Gas Adsorption Analyzer.

The surface composition and depth profile of WO_3-doped $LiMn_{1.5}Ni_{0.5}O_4$ particles were characterized by both XPS and Auger electron spectroscopy (AES). XPS was carried out by using a Kratos AXIS ULTRA DLD XPS system equipped with an Al Kα monochromated X-ray source and a 165 mm mean radius electron energy hemispherical analyzer with a step size of 0.1 eV. A 4 keV Ar ion beam was used for sputtering. Binding energies were corrected using C 1s peak 284.6 eV. The sample current was set to be ~4 μA. Depth profile data were collected after sputtering times of 10, 30, 60, 120, and 240 s. The measured XPS depth profiles represent averages of many different particles and crystalline facets. The XPS data were fitted with the XPSPEAK41 software.

AES surface analysis, in conjunction with depth profiling using ion sputtering, was carried out by a PHI 700 scanning Auger nanoprobe with a nanoscale spatial resolution to obtain surface compositions of individual crystalline facets. Au foils were used as substrates to eliminate charging effects. A multiplex mode survey was used to acquire accurate quantitative results of various elements on surface. The signals from O, Mn, Ni, and W, respectively, were scanned in ranges of 496.4−532.0 eV, 557.8−611 eV, 811−871 eV, and 1692.5−1758.8 eV, respectively, and subsequently analyzed in ranges of 502.7−526.5 eV, 563.9−604.5 eV, 824.1−863.0 eV, and 1713.0−1748.9 eV, respectively. Each test was carried out with 40 sweeps and 1 eV per step. Ten cycles of measurements were conducted to obtain high-quality signals, in which the acquisition area was corrected after each point test to avoid beam drift and ensure that data was acquired in the same location. The Mn2 signal at 536 eV was selected since there is an overlap of the Mn1 (519 eV) and O (510 eV) signals. Elemental compositions on the facets of (100), (110), and (111) of W-doped and undoped $LiMn_{1.5}Ni_{0.5}O_4$ specimens were investigated. At least two points were taken on each facet. A beam energy of 20 kV was used to get a smaller beam size with a spatial resolution of about 8−10 nm. The sputtering source was neutralized Ar of 1 kV beam energy with a 30° incident angle with the sample. The target emission current was 15 mA. The sputtering area was 1 mm × 1 mm. The sputter time was 30 s (between collecting two data points) with a delay of 3 s. The specimen position was recalibrated after each spot was measured. The AES data were fitted with the MultiPak software.

Neutron diffraction characterization data were collected on the VULCAN beamline at the Spallation Neutron Sources (SNS) in the Oak Ridge National Laboratory (ORNL). An incident beam (5 mm × 12 mm) of 0.7−3.5 Å bandwidth, allowing 0.5−2.5 Å d-space in diffracted patterns in the $\theta \pm 90°$ detector banks, was selected using the double-disk choppers at a 30 Hz speed. The high-resolution mode was employed with $\Delta d/d \approx 0.25\%$. The SNS power was at 1100 KW nominally. Neutron diffraction data were collected for a duration of 3 h[43,44] at room temperature and were reduced by the VDRIVE software.[45,46] A full-pattern Rietveld refinement was performed using the GSAS programs with the EXPGUI interface.[47,48]

To prepare cathodes, 80 wt % active materials, 15 wt % carbon black (MTI), 5 wt % PVDF (MTI), and an appropriate amount of NMP (Alfa Aesar, anhydrous, 99.5%) were mixed in a glass vial by a vibrating mixer, followed by ultrasonic dispersion. The mixture was coated on

DOI: 10.1021/acsami.7b09903
ACS Appl. Mater. Interfaces 2017, 9, 36745−36754

an aluminum foil, which was subsequently dried in a vacuum oven at 90 °C for 6 h. Cathode electrodes with a diameter of 10 mm were punched out, pressed at ~187 MPa, and dried in a vacuum oven at 120 °C for 8 h before transferring into an Ar-filled glovebox for battery construction. The density of dried electrode coating was ~3.2 mg cm^{-2}. Half-cells were made with a cathode electrode, a metal Li chip (MTI, 99.9%) as the anode, 1 M $LiPF_6$ in 1:1 vol. EC/DMC electrolyte (LP 30, BASF), C480 separators (Celgard), and 2032 coin cell cases (SS304, MTI).

Electrochemical cycling tests were carried out on an Arbin 2143 tester. The rate performance of $LiMn_{1.5}Ni_{0.5}O_4$ specimens was tested at the discharge rates of C/10, C/5, 1C, 5C, 25C, 45C, 65C, and 85C sequentially (with 4 cycles at C/5 to stabilize the battery and 1 cycle for other discharge rates subsequently; 1C equates to 150 mA g^{-1}) with a constant charge rate of C/5 at room temperature. The cycling stability of $LiMn_{1.5}Ni_{0.5}O_4$ specimens were measured at charge and discharge rate of 1C between 3.2 and 5.0 V at an elevated temperature of 55 ± 3 °C in a dry oven after first idling at 55 ± 3 °C for 2 h.

Cyclic voltammetry (CV) and electrochemical impedance spectroscopy (EIS) were performed using a Solartron 1287A/1255B analyzer. CV was performed between 3.2 and 5.0 V at a scan rate of 0.1 mV s^{-1}. EIS spectra were measured from 1 MHz to 0.05 Hz at 10 mV. The EIS data were fitted with the ZView software. The cells after rate capability test were charged to a cutoff voltage of 5.0 V at C/10 and kept for 10 h for the subsequent impedance measurements.

3. RESULTS

3.1. Surface Areas and Particle Morphologies. The measured BET-specific surface areas of the undoped and WO_3-doped $LiMn_{1.5}Ni_{0.5}O_4$ specimens prepared using identical ball-milling and annealing conditions were ~1.8 and ~1.7 m^2/g, respectively, a difference of only ~6%; the undoped $LiMn_{1.5}Ni_{0.5}O_4$ specimen had a slightly larger specific surface area. The comparable BET specific surface areas ensured fair comparisons so that the enhanced rate capability and cycling stability of the WO_3-doped $LiMn_{1.5}Ni_{0.5}O_4$ specimen as compared to those of the undoped specimen (that will be discussed subsequently) were not due to different specific surface areas.

The morphologies of the undoped and WO_3-doped $LiMn_{1.5}Ni_{0.5}O_4$ particles are shown in Figure 1, where some

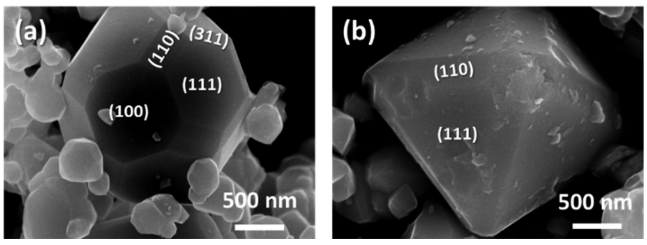

Figure 1. Representative SEM images of the (a) undoped and (b) 1 vol % WO_3-doped $LiMn_{1.5}Ni_{0.5}O_4$ specimens, where were prepared by annealing high-energy ball-milled powders at 800 °C for 4 h.

differences are evident. For the undoped $LiMn_{1.5}Ni_{0.5}O_4$ particles, surface facets of {111}, {110}, {100}, and {311} coexisted, with estimated surface area fractions of ~44, ~18, ~20, and ~18%, respectively, which were calculated from Wulff construction simulation of a particle (Figure 2a) that matched the observation by SEM (Figure 1a). These observed results are generally consistent with prior density functional theory (DFT) computations.[36] For the WO_3-doped $LiMn_{1.5}Ni_{0.5}O_4$ particles, the surface area fraction of the {111} facets increased slightly from ~44 to ~56%, and the fraction of the {110} facets

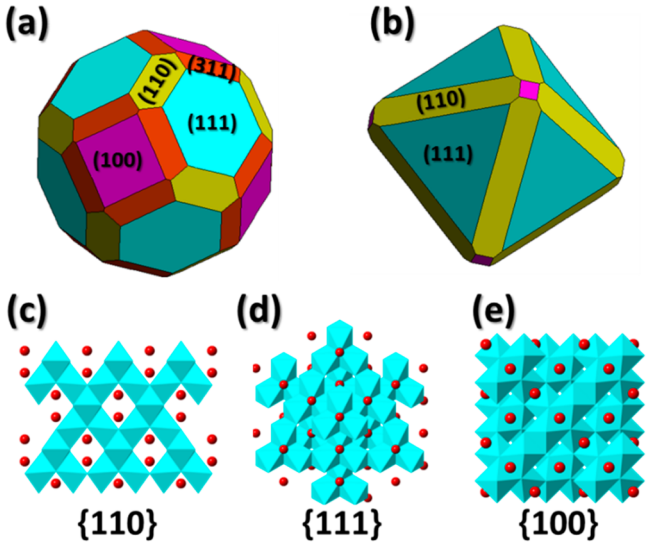

Figure 2. Calculated Wulff shapes of the (a) undoped and (b) WO_3-doped $LiMn_{1.5}Ni_{0.5}O_4$ that matched the experimentally observed particle morphologies shown in Figure 1 and schematics of the Li ion diffusion channels on (c) {110}, (d) {111}, and (e) {100} facets, respectively. Red dots and blue octahedra represent Li ions and MO_6 (M = Mn, Ni), respectively. The relative surface energies that produced these Wulff shapes are listed in Table 1.

increased substantially from ~18 to ~43%. The fraction of the {100} facets decreased drastically from ~20 to <2%, and the {311} facets disappeared completely. The surface area fraction of the {110} facets had the largest increase, being more than doubled with WO_3 doping.

The simulation of Wulff shapes was done with the software Wulffmaker running in Wolfram CDF Player.[49] The simulated Wulff crystals of the undoped and WO_3-doped $LiMn_{1.5}Ni_{0.5}O_4$ that matched the crystal morphologies observed by SEM (Figure 1) are shown in Figure 2a,b, respectively, and corresponding relative surface energies are listed in Table 1. In comparison with that of the {100} facets, the surface energies of both {111} and {110} facets decreased more rapidly with WO_3 adsorption.

Table 1. Relative Surface Energies of the Undoped and WO_3-Doped $LiMn_{1.5}Ni_{0.5}O_4$ Specimens that Matched the Experimentally Observed Wulff Shapes

	undoped	WO_3-doped
$\gamma_{\{111\}}/\gamma_{\{100\}}$	0.94	0.69
$\gamma_{\{110\}}/\gamma_{\{100\}}$	1.04	0.76
$\gamma_{\{311\}}/\gamma_{\{100\}}$	1.05	

3.2. Anisotropic Surface Segregation. Strong surface segregation of W was clearly evident in the XPS depth profile. As shown in Figure 3, the surface atomic ratio of W/Mn was measured by XPS to be 0.23 ± 0.01 based on the fitting results, which decreased rapidly with ion sputtering to ~0.07 after 60 s and leveled off at ~0.03 after sputtering 240 s (while the overall nominal W/Mn ratio is 0.06). The surface Ni/Mn ratio was measured to be 0.23 ± 0.07, which was substantially lower than the nominal bulk Ni/Mn ratio of $^1/_3$. After sputtering for 60 s, the measured atomic ratio of W/Mn is 0.33 ± 0.04, approaching to the nominal bulk stoichiometric ratio of $^1/_3$ and stayed roughly constant. The sputtering rate was calibrated

DOI: 10.1021/acsami.7b09903
ACS Appl. Mater. Interfaces 2017, 9, 36745−36754

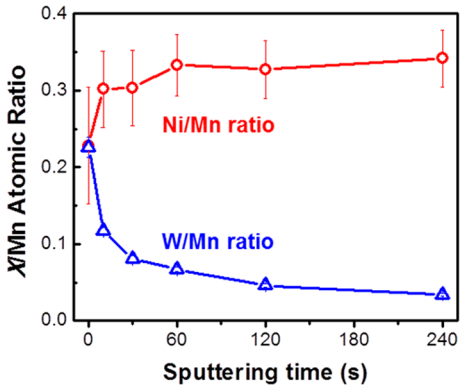

Figure 3. Atomic ratios of W/Mn and Ni/Mn vs sputtering time curves measured from XPS.

to be about 30 nm min^{-1} when a reference SiO_2 material was sputtered at the same experimental condition.[50]

Furthermore, AES with a nanoprobe of ~10 nm in the beam size was employed to quantitatively analyze the W atomic ratios on various facets to identify anisotropy in surface segregation. The measured depth profiles of W (obtained by ion sputtering) on the facets {110}, {100}, and {111} are shown in Figure 4.

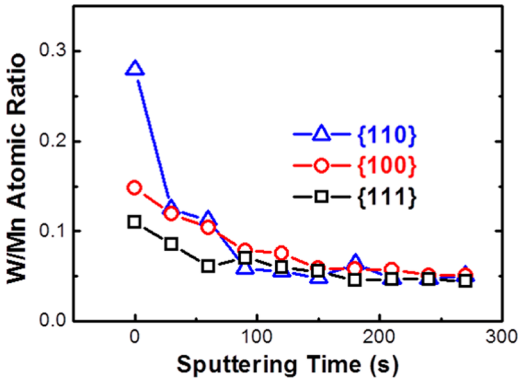

Figure 4. Atomic ratios of W to Mn vs. sputtering time curves measured by AES on three different surface facets of {110}, {100}, and {111}. The {110} facet has the highest level of W segregation, which is consistent with the observed largest reduction in the relative surface energy in the WO_3-doped specimen (Table 1).

The atomic ratios of W/Mn on {110}, {100}, and {111} facets, respectively, before sputtering was 0.28, 0.15, and 0.11, respectively. The surface of the {110} facet had the highest W/Mn atomic ratio of 0.28, which was 1.8-fold that on the {100} facet and 2.4-fold that the {111} facet, respectively. The atomic ratios of W/Mn on all facets decreased with increasing sputtering time and leveled off after sputtering for 90 s. The sputtering rate was calibrated to be ~5 nm min^{-1} for a reference material of Si for using 1 kV Ar. Finally, the atomic ratio of W/Mn on various facets all converged to ~0.05 after sputtering for 240 s, close to the XPS result. The AES depth profiles clearly indicate that W prefers to segregate on {110} facets, in comparison with behavior on {100} and {111} facets.

It is worth noting that we used terminology "WO_3 doping" (instead of "WO_3 coating") here because the materials were prepared by a "mixing and annealing" synthesis route and WO_3 segregated at surfaces spontaneously (driven by thermodynamics) in a chemical/thermodynamically equilibrium with the WO_3-doped bulk material.

3.3. Electrochemical Performances. The rate capability of $LiMn_{1.5}Ni_{0.5}O_4$ was enhanced significantly by WO_3 doping. Figure 5a showed the comparison of rate capabilities between undoped and doped specimens; it is worth noting that the changes in the discharge capacities in Figure 5a were mainly related to the changes in the testing rates, as different rates (and labeled in Figure 5a) were used in each cycle. The discharge capacities of the doped specimen were substantially higher than those of the undoped specimen at all rates. Specifically, the difference in the discharge capacities between doped and undoped specimens increased with the increasing rate from 1C to 25C. At 25C, undoped $LiMn_{1.5}Ni_{0.5}O_4$ only had an average discharge capacity of 16.6 ± 24.3 mAh g^{-1}; in contrast, the WO_3-doped $LiMn_{1.5}Ni_{0.5}O_4$ maintained an average discharge capacity of 101.3 ± 0.4 mAh g^{-1}, representing an ~500% increase from the undoped specimen. Furthermore, at rates higher than 25C, the undoped specimen exhibited virtually no discharge capacity (<1 mAh g^{-1}), but the WO_3-doped specimen still retained discharge capacities of 79.4 ± 5.6 mAh g^{-1} at 45C, 46.9 ± 16.8 mAh g^{-1} at 65C, and 13.8 ± 2.4 mAh g^{-1} at 85C, respectively. Though a relatively low mass loading of 3.2 mg/cm^2 with 80% active material was used in this study, outstanding rate performance could still be achieved by optimizing the carbon content for a thick electrode.

The measured EIS spectra are shown in Figure 6 and fitted results are displayed in Table 2. Both the surface film and charge transfer resistances decreased from 156.0 and 47.0 Ω of the undoped specimen to 56.3 and 19.5 Ω of the doped specimen, which is consistent with the enhanced rate performance. The decrease of the charge transfer resistance (Figure 6) could be related to the increase of {110} surface facets that may be favorite for the surface charge and ion transfer.

Figure 7 displays the charge and discharge profiles of the doped and undoped specimens in the first cycle at C/10. The discharge capacity of the doped $LiMn_{1.5}Ni_{0.5}O_4$ is 132.6 mAh g^{-1}, which was higher than 116.9 mAh g^{-1} of the undoped $LiMn_{1.5}Ni_{0.5}O_4$. The increase of discharge capacity of ~16 mAh g^{-1} in the WO_3-doped specimen is mainly resulted from the extended $Ni^{2+/4+}$ plateau (at ~4.6 and ~4.8 V) and $Mn^{3+/4+}$ plateau (at ~4.0 V), indicating increased amounts of $Ni^{2+/4+}$ and $Mn^{3+/4+}$ redox couples.[3,51] This observation is consistent with measured CV results shown in Figure 8. Specifically, the discharge capacity contributed by $Mn^{3+/4+}$ (3.60–4.25 V) and $Ni^{2+/4+}$ (4.25–4.8 V) in the doped specimen increased by 6.6 mAh g^{-1} (from 10.4 to 17.0 mAh g^{-1}) and 10.8 mAh g^{-1} (from 104 to 114.8 mAh g^{-1}), respectively, in comparison to those of the undoped $LiMn_{1.5}Ni_{0.5}O_4$. In addition, the Coulombic efficiency of the first cycle was also improved from 78 to 86% with WO_3 doping, leading to a difference of the initial discharge capacity between undoped and doped specimens.

Figure 9 shows that the cycling performance was also enhanced by WO_3 doping. After 200 cycles at an elevated temperature of 55 °C and a relatively high rate of 1C, the discharge capacities were 111.7 and 88.9 mAh g^{-1}, respectively, for the doped and undoped specimens, respectively, corresponding to capacity retentions of 87 and 81%, respectively. Hence, the significant improvement of the discharge capacity of doped specimen after 200 cycles was mainly attributed to the increase in the initial reversible capacity by WO_3 surface segregation. Both the rate capability and cycling stability of the undoped specimen obtained in this work are comparable with

DOI: 10.1021/acsami.7b09903
ACS Appl. Mater. Interfaces 2017, 9, 36745–36754

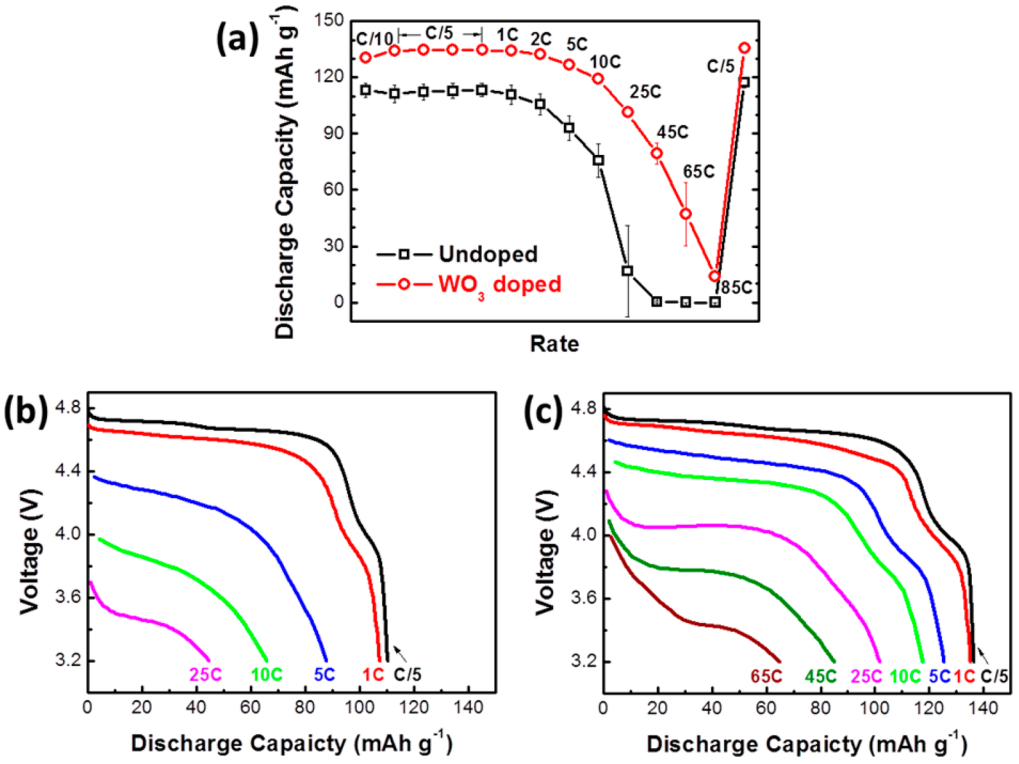

Figure 5. (a) Comparison of rate performancesof undoped and WO_3-doped $LiMn_{1.5}Ni_{0.5}O_4$ specimens and discharge curves of (b) undoped specimen and (c) WO_3-doped $LiMn_{1.5}Ni_{0.5}O_4$ specimens. Three coin cells were made and tested for each specimen. The means are presented in the graph and error bars represent ± 1 standard deviations. All cells were first charged and discharged at C/10 for 1 cycle and C/5 for 4 cycles to reach steady states and subsequently charged at C/5 and discharged at various rates (labeled in the graph) at room temperature.

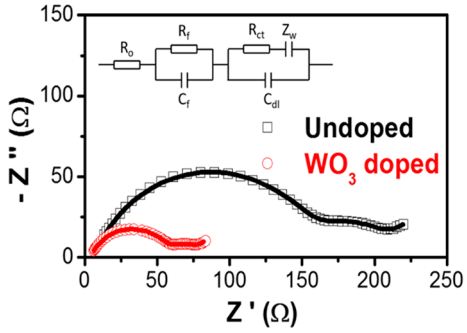

Figure 6. Measured EIS spectra of the undoped and WO_3-doped (red circles) $LiMn_{1.5}Ni_{0.5}O_4$ specimens. The inset is an equivalent circuit. The fitted surface film and charge transfer resistances are given in Table 2.

Table 2. Fitted Surface Film and Charge Transfer Resistances from EIS

specimen	R_f (Ω)	R_{ct} (Ω)
undoped	156.0 ± 0.7	47.0 ± 1.9
WO_3-doped	56.3 ± 0.3	19.5 ± 1.0

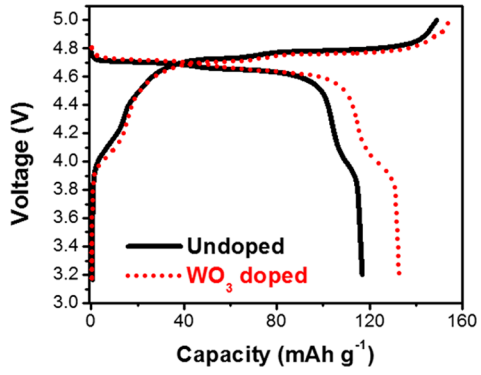

Figure 7. Measured charge/discharge curves for the undoped and WO_3-doped $LiMn_{1.5}Ni_{0.5}O_4$ specimens. Both specimens were charged and discharged at a low rate of 0.1C at room temperature.

those previously reported with the same/similar compositions and loading density of the active material.[30]

3.4. Surface and Bulk Mn^{3+} Concentrations. XPS characterization of the Mn cations of the WO_3-doped specimen as a function of sputtering time (labeled in the graph) is shown in Figure 10a, where a decrease in the binding energy represents a decrease of the cation valence. Specifically, the Mn 2p binding energy shifted from 641.8 eV at the surface to 640.3 eV in the bulk, suggesting that the average Mn valence at the surface is higher. In other words, the Mn^{3+} concentration on the surface was likely lower than that in the bulk. This result is different from the reported result of the undoped $LiMn_{1.5}Ni_{0.5}O_4$, where no shift in the Mn 2p binding energy after sputtering implies no change of the Mn valence at the surface.[50]

For W, the distance between the two spin−orbit split doublets, W $4f_{5/2}$ and W $4f_{7/2}$, is 2.15 eV, and the area ratio is 4:3, both of which should be constant (as required by quantum mechanics). As shown in Figure 10b, the W $4f_{7/2}$ peak was at ~34.7 eV in the XPS spectrum before sputtering and shifted by ~0.2 eV toward higher energies after sputtering. The lower peak energies suggest the presence of some W^{5+} on the surface, while the shift to a higher binding energy with sputtering time

DOI: 10.1021/acsami.7b09903
ACS Appl. Mater. Interfaces 2017, 9, 36745−36754

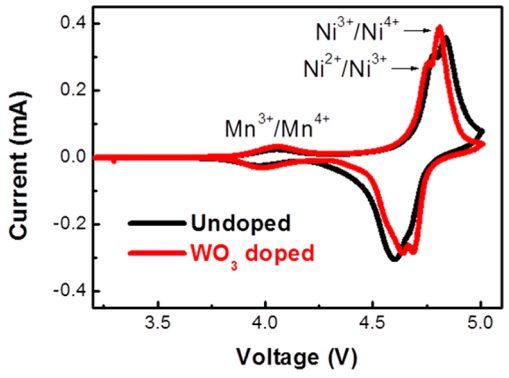

Figure 8. Measured CV curves of the undoped and WO_3-doped $LiMn_{1.5}Ni_{0.5}O_4$ specimens.

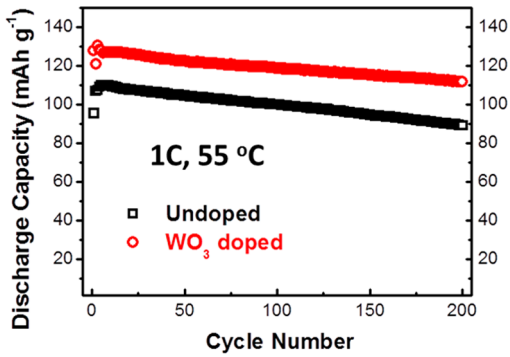

Figure 9. Cycling stability results of the undoped and WO_3-doped doped $LiMn_{1.5}Ni_{0.5}O_4$ specimens tested at an elevated temperature of 55 °C with a relatively high charge and discharge rate of 1C as an accelerated test.

implies more oxidized states of tungsten (presumably W^{6+}) in the bulk phase. The more reduced valence state of W ($W^{6+} \rightarrow W^{5+}$) is likely correlated with more oxidized state of Mn ($Mn^{3+} \rightarrow Mn^{4+}$) at the surface, which presumably helps to reduce the dissolution of Mn and improve the cycling stability. In addition, the Ni $2p_{3/2}$ binding energy was ~854.2 eV, which is consistent with that reported in literature,[50,52] and did not change with the sputtering time, indicating that the Ni valence does not change at the surface.

3.5. Neutron Diffraction. Figure 11 shows the neutron diffraction patterns for the undoped and WO_3-doped $LiMn_{1.5}Ni_{0.5}O_4$ specimens. The Rietveld refinement structure analysis was used to investigate the crystal structure of both samples.[53−56] For long-term annealing at 700 °C, $LiMn_{1.5}Ni_{0.5}O_4$ intended to become ordered structure, and the ordered structure is disturbed upon further higher heating.[57,58] While these samples were annealed at 800 °C and cooled down quickly, both of them retained the fully disordered structure. Both patterns of undoped and doped specimens did not show any superstructure peaks arising from ordered structure ($P4_332$ space group), and both were successfully refined according to the $Fd\bar{3}m$ space group of a disordered structure. The corresponding reliable factors R_{wp} and R_p are 3.76 and 2.89% for the undoped specimen, and they were 3.36 and 2.47% for the doped specimen. The lattice constants were 8.1610 ± 0.0003 and 8.1662 ± 0.0002 Å, respectively, for the undoped and doped specimens, respectively. An increase in the lattice constant (0.0052 Å) after WO_3 doping was observed.

A secondary phase indexed with a rock-salt structure ($Fm\bar{3}m$ space group) was found in both patterns.[58] The impurity content was 0.82 ± 0.07 wt % for the undoped specimen and 1.83 ± 0.08 wt % for the doped specimen. The influence of such small amounts of the impurity phase on the electro-

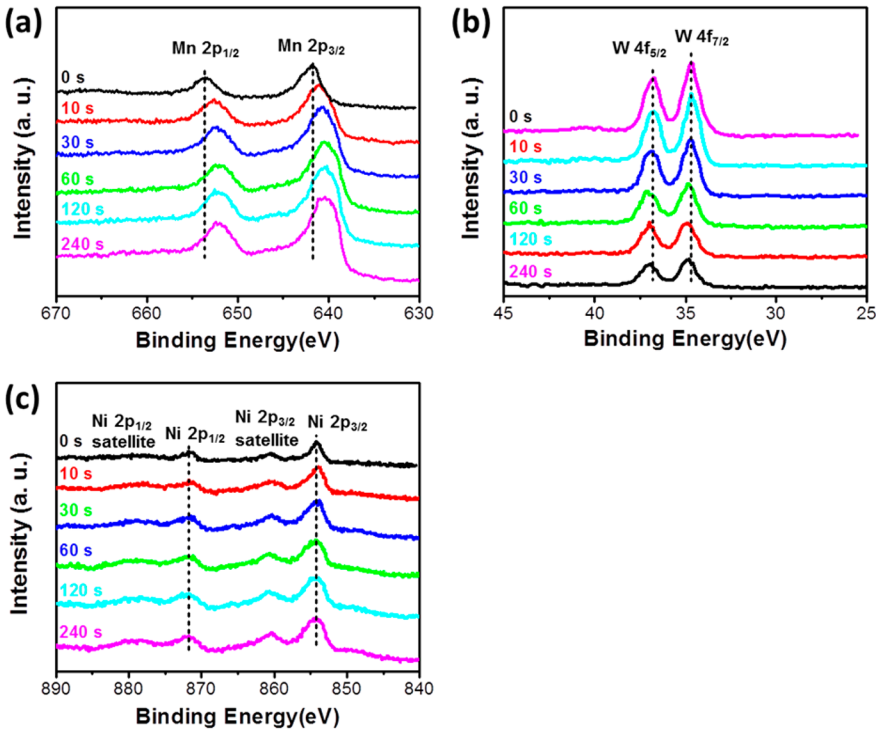

Figure 10. XPS results of (a) Mn, (b) W, and (c) Ni binding energy shifts after sputtering for different times (labeled in the graphs) for the 1 vol % WO_3-doped $LiMn_{1.5}Ni_{0.5}O_4$ specimen.

DOI: 10.1021/acsami.7b09903
ACS Appl. Mater. Interfaces 2017, 9, 36745−36754

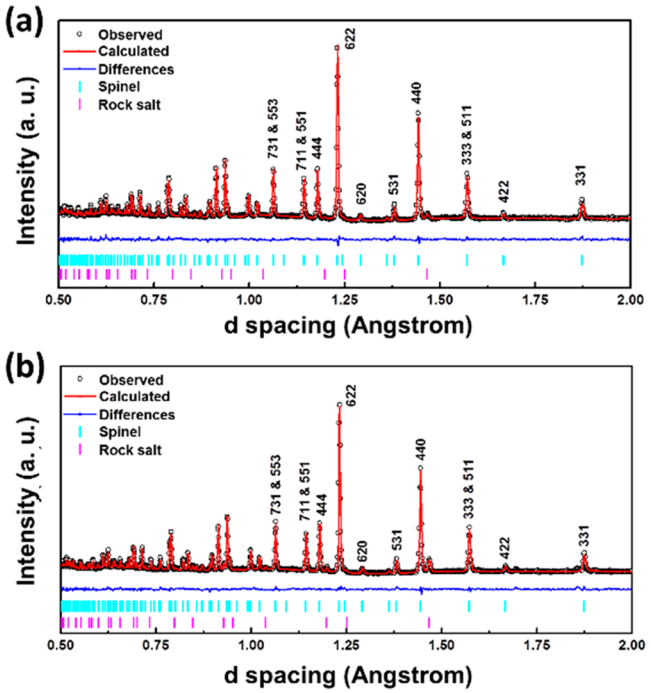

Figure 11. Neutron powder diffraction patterns of the (a) undoped and (b) 1 vol % WO_3-doped $LiMn_{1.5}Ni_{0.5}O_4$ specimens.

chemical performance may be negligible. WO_3 doping also decreased the oxygen occupancy from 100.6 ± 1.8 to 97.7 ± 1.5%, which is consistent with the increased concentration of Mn^{3+} in the bulk phase, as well as the slight increase in the lattice constant.

4. DISCUSSION

4.1. Change in Particle Morphology and Anisotropic Surface Segregation of W. Both undoped and doped specimens were prepared via the same procedure except for the addition of WO_3. The resultant particle sizes (Figure 1) and BET surface areas of undoped and doped specimens were roughly identical within the measurement errors. Hence, it is reasonable to assume that WO_3 doping led to the change in particle morphology (Figures 1 and 2a,b).

Furthermore, both XPS and AES have unequivocally demonstrated the surface segregation (adsorption) of W in the doped $LiMn_{1.5}Ni_{0.5}O_4$ particles. The surface energy can be changed (reduced) with adsorption/segregation of W according to the well-known Gibbs adsorption equation:

$$\frac{d\gamma}{d\mu} = -\Gamma \quad (1)$$

where γ is the surface energy, and μ and Γ, respectively, are the chemical potential and surface excess (total adsorption amount per unit area) of the adsorbing specie, respectively. Furthermore, AES depth profiles (Figure 4) show that W prefers to segregate at the {110} surface facets (with a greater Γ), which leads to a greater reduction of $\gamma_{\{110\}}$ in comparison with that of other facets. Consequently, the largest reduction in the relative surface energy in $\gamma_{\{110\}}$ (Table 1) leads to an increase in the fraction of the {110} facets according to the well-established Wulff theory (construction) of the equilibrium crystal shape, which are consistent with experimental observations (Figures 1 and 2a,b). Similarly, anisotropic segregation may also destabilize {311} facets and change the relative ratios of other facets.

4.2. Mechanisms of the Improved Rate Capability. The increase fraction of the {110} (as well as {111}) facets may enhance the rate capability because {110} (as well as {111}) facets exhibit more open channels for fast diffusion of Li^+ ions (Figure 2c–e). Though $LiMn_{1.5}Ni_{0.5}O_4$ is regarded as a 3D lithium diffusion material, the lithium diffusion rates perpendicular to different facets can be different, particularly at high charging and discharging rates. As shown in Figure 2c–e, the {110} facets provide the most open path for the lithium diffusion, followed by the {111} facets and then the {100} facets. Since the anisotropic surface segregation of W significantly increased the fraction of the {110} facets (from ~18 to ~43%) and moderately increased the fraction of the {111} facets (from ~44 to ~56%), as shown in Figures 1 and 2a,b, it improved the rate performance of the doped specimen (Figure 5).

We note that the bulk doping of W^{6+} can increase the concentration of Mn^{3+} in the bulk phase, which can also improve the rate capability via triggering cation disordering in $LiMn_{1-x}Ni_xO_4$ (being a possible alternative mechanism for the improved rate performance).[7] However, if the structure is (already) disordered, then further increasing the Mn^{3+} content in the disordered structure may not further improve the rate capability.[7] In the current case, refined structures obtained from neutron diffraction (Figure 11) suggested that both undoped and doped specimens are likely fully disordered. Hence, the increase of the Mn^{3+} concentration in the bulk phase of the doped specimen may not play a major role in improving the rate capability in the current case. In other words, the improved rate capability in the current case is mostly likely related to the anisotropic surface segregation of W and the associated particle morphological change of the Wulff shape with increased fractions of the favorite {110}, as well as {111}, facets. In addition to improving the cycling stability (a subject that will be discussed further in the next section), the improved the chemical stability of the W-segregated surfaces can also improve the rate capability via suppressing the rapid increase of the surface resistance, as evident directly in EIS results (Figure 6).

4.3. Mechanisms of the Increased Discharge Capacity and Cycling Stability. The neutron diffraction results showed evidence of increased oxygen vacancy concentration as well as an increased lattice constant with the W doping, implying an increase of the Mn^{3+} concentration in the bulk phase of the WO_3-doped $LiMn_{1.5}Ni_{0.5}O_4$ specimen. It is known that an increased Mn^{3+} content can contribute to an increasing specific capacity at the voltage plateau ~4 V (Figure 7).[9] It is also known that the existence of Mn^{3+} on the surface can trigger disproportionation of Mn^{3+} cations to Mn^{2+} and Mn^{4+} cations, which can promote the dissolution of Mn^{2+} in the electrolyte and subsequently capacity losses; subsequently, the Mn^{3+} concentration on the surface can increase further during electrochemical cycling, which can further promote the dissolution of Mn^{2+}, resulting in poor cycling stability.[59]

However, our cycling stability results (Figure 9) clearly show that the doped specimen (that presumably have a high Mn^{3+} content) had a better cycling stability than the undoped specimen. This is likely related to the W surface segregation (along with the partial reduction of W^{6+} to W^{5+} at the surface; Figure 10b), which likely decreases the Mn^{3+} concentration at the surface, thereby enhancing the cycling stability via reducing

DOI: 10.1021/acsami.7b09903
ACS Appl. Mater. Interfaces 2017, 9, 36745–36754

the disproportionation of Mn^{3+} cations and suppressing the Mn^{2+} dissolution.

We note that a most recent report by Kuppan et al. suggested "superior kinetics of (100) facets at the vertices of truncated octahedral particles" can promote anisotropic (preferential) delithiation that cause degradation due to strain-induced cracking in larger (micrometer-sized) particles.[60] In our case, WO_3 segregation increased the fractions of both {110} and {110} planes but reduced the fraction of {100} facets, which could also be beneficial and contributed to the increased cycling stability.

In summary, W^{6+} doping in the bulk phase introduces oxygen vacancies and increases the bulk Mn^{3+} concentration, which can enhance the specific discharge capacity. The surface segregation and partial reduction of W at surface reduce the surface Mn^{3+} concentration, which may increase the cycling stability by suppressing the formation and dissolution of Mn^{2+} at the surfaces (along with the possible beneficial effects of the surface segregation of W).

This beneficial surface configuration (with W segregation and partial reduction, along with suppressed Mn^{3+} concentration at/near the surface) that spontaneously formed during mixing and annealing in the WO_3-doped $LiMn_{1.5}Ni_{0.5}O_4$ specimen (as the thermodynamically equilibrium surface state) is a 2-D surface phase (also called "complexion")[61,62] that can be considered as naturally formed surface protective "coatings," akin to those nanoscale surface amorphous films[63−66] or nitridated surfaces[67] observed in prior studies that also improved both the rate capabilities[63,64,66,67] and cycling stabilities[63] of a range of battery cathode[63,64,66] and anode[67] materials.

5. CONCLUSIONS

Minor WO_3 doping, which can be achieved by a facile ball-milling and annealing process, can substantially enhance the electrochemical performance of $LiMn_{1.5}Ni_{0.5}O_4$, and in this study, we depict the underlying mechanisms of improved ionic transport and CEI stability via combining neutron diffraction, an Auger electron nanoprobe, X-ray photoelectron spectroscopy, and other characterizations.

While the W^{6+} doping in the bulk phase leads to extra oxygen vacancies and an increase of the bulk Mn^{3+} concentration, the surface segregation and partial reduction of W reduce the surface Mn^{3+} concentration, which improves the cycling stability via reducing the surface disproportionation of Mn^{3+} cations and suppressing the subsequent dissolution of Mn^{2+} cations. Furthermore, anisotropic surface segregation of W changes the relative surface energies of different crystalline facets and subsequently the Wulff shape of the crystalline particles, which improves the rate capability via increasing the areas of {110} and {111} facets with more open channels for fast lithium ion diffusion. For example, the discharge capacity at 25C can be increased by ~500% by 1 vol % WO_3 doping.

In a broader context, this study has demonstrated the anisotropic surface segregation (or formation of 2D surface phases[63−67] in general) can be utilized as a facile method to control the particle morphology thermodynamically, as well as modify surface properties (i.e., increase the electrochemical stability and surface transport rates in this particular case), to significantly improve the rate capability, cycling stability, and potentially other properties of battery materials, as well as a broad range of other functional materials for energy-related applications, such as supercapacitors[68] and photocatalysts.[69,70]

AUTHOR INFORMATION

Corresponding Author

*E-mail: jluo@alum.mit.edu.

ORCID

Ying Shirley Meng: 0000-0001-8936-8845

Jian Luo: 0000-0002-5424-0216

Notes

The authors declare no competing financial interest.

ACKNOWLEDGMENTS

This work was partially supported by a Vannevar Bush Faculty Fellowship sponsored by the Basic Research Office of the Assistant Secretary of Defense for Research and Engineering and funded by the Office of Naval Research through grant N00014-16-1-2569. H.L. and Y.S.M. acknowledge the partial support by the U.S. Department of Energy, Office of Basic Energy Sciences, under Award Number DE-SC0002357. We thank Dr. Lee Ilkeun and Prof. Zaera from University of California Riverside for collecting the XPS data using the instrument funded by the U.S. National Science Foundation under the Major Research Instrumentation Program through grant DMR-0958796. The neutron experiments benefited from the SNS user facility, sponsored by the office of Basic Energy Sciences (BES), the Office of Science of the DOE.

REFERENCES

(1) Idemoto, Y.; Narai, H.; Koura, N. Crystal Structure and Cathode Performance Dependence on Oxygen Content of $LiMn_{1.5}Ni_{0.5}O_4$ as a Cathode Material for Secondary Lithium Batteries. *J. Power Sources* **2003**, *119−121*, 125−129.

(2) Kunduraci, M.; Al-Sharab, J. F.; Amatucci, G. G. High-Power Nanostructured $LiMn_{2-x}Ni_xO_4$ High-Voltage Lithium-Ion Battery Electrode Materials: Electrochemical Impact of Electronic Conductivity and Morphology. *Chem. Mater.* **2006**, *18*, 3585−3592.

(3) Kunduraci, M.; Amatucci, G. G. The Effect of Particle Size and Morphology on the Rate Capability of 4.7 V $LiMn_{1.5+\delta}Ni_{0.5-\delta}O_4$ Spinel Lithium-Ion Battery Cathodes. *Electrochim. Acta* **2008**, *53*, 4193−4199.

(4) Cabana, J.; Casas-Cabanas, M.; Omenya, F. O.; Chernova, N. A.; Zeng, D.; Whittingham, M. S.; Grey, C. P. Composition-Structure Relationships in the Li-Ion Battery Electrode Material $LiNi_{0.5}Mn_{1.5}O_4$. *Chem. Mater.* **2012**, *24*, 2952−2964.

(5) Shin, D. W.; Bridges, C. A.; Huq, A.; Paranthaman, M. P.; Manthiram, A. Role of Cation Ordering and Surface Segregation in High-Voltage Spinel $LiMn_{1.5}Ni_{0.5-x}M_xO_4$ (M = Cr, Fe, and Ga) Cathodes for Lithium-Ion Batteries. *Chem. Mater.* **2012**, *24*, 3720−3731.

(6) Xiao, J.; Chen, X.; Sushko, P. V.; Sushko, M. L.; Kovarik, L.; Feng, J.; Deng, Z.; Zheng, J.; Graff, G. L.; Nie, Z.; Choi, D.; Liu, J.; Zhang, J.-G.; Whittingham, M. S. High-Performance $LiNi_{0.5}Mn_{1.5}O_4$ Spinel Controlled by Mn^{3+} Concentration and Site Disorder. *Adv. Mater.* **2012**, *24*, 2109−2116.

(7) Duncan, H.; Hai, B.; Leskes, M.; Grey, C. P.; Chen, G. Relationships between Mn^{3+} Content, Structural Ordering, Phase Transformation, and Kinetic Properties in $LiNi_xMn_{2-x}O_4$ Cathode Materials. *Chem. Mater.* **2014**, *26*, 5374−5382.

(8) Tarascon, J. M.; McKinnon, W. R.; Coowar, F.; Bowmer, T. N.; Amatucci, G.; Guyomard, D. Synthesis Conditions and Oxygen Stoichiometry Effects on Li Insertion into the Spinel $LiMn_2O_4$. *J. Electrochem. Soc.* **1994**, *141*, 1421−1431.

(9) Song, J.; Shin, D. W.; Lu, Y.; Amos, C. D.; Manthiram, A.; Goodenough, J. B. Role of Oxygen Vacancies on the Performance of $Li[Ni_{0.5-X}Mn_{1.5+X}]O_4$ (X = 0, 0.05, and 0.08) Spinel Cathodes for Lithium-Ion Batteries. *Chem. Mater.* **2012**, *24*, 3101−3109.

DOI: 10.1021/acsami.7b09903
ACS Appl. Mater. Interfaces 2017, 9, 36745−36754

(10) Zhong, Q.; Bonakdarpour, A.; Zhang, M.; Gao, Y.; Dahn, J. R. Synthesis and Electrochemistry of $LiNi_XMn_{2-X}O_4$. *J. Electrochem. Soc.* **1997**, *144*, 205−213.
(11) Chong, J.; Xun, S.; Song, X.; Liu, G.; Battaglia, V. S. Surface Stabilized $LiNi_{0.5}Mn_{1.5}O_4$ Cathode Materials with High-Rate Capability and Long Cycle Life for Lithium Ion Batteries. *Nano Energy* **2013**, *2*, 283−293.
(12) Huang, J.; Luo, J. A Facile and Generic Method to Improve Cathode Materials for Lithium-Ion Batteries Via Utilizing Nanoscale Surface Amorphous Films of Self-Regulating Thickness. *Phys. Chem. Chem. Phys.* **2014**, *16*, 7786−7798.
(13) Aklalouch, M.; Rojas, R. M.; Rojo, J. M.; Saadoune, I.; Amarilla, J. M. The Role of Particle Size on the Electrochemical Properties at 25 and at 55 °C of the $LiCr_{0.2}Ni_{0.4}Mn_{1.4}O_4$ Spinel as 5 V-Cathode Materials for Lithium-Ion Batteries. *Electrochim. Acta* **2009**, *54*, 7542−7550.
(14) Wang, H.; Xia, H.; Lai, M. O.; Lu, L. Enhancements of Rate Capability and Cyclic Performance of Spinel $LiNi_{0.5}Mn_{1.5}O_4$ by Trace Ru-Doping. *Electrochem. Commun.* **2009**, *11*, 1539−1542.
(15) Zhong, G. B.; Wang, Y. Y.; Zhao, X. J.; Wang, Q. S.; Yu, Y.; Chen, C. H. Structural, Electrochemical and Thermal Stability Investigations on $LiNi_{0.5-x}Al_{2x}Mn_{1.5-x}O_4$ ($0 \le 2x \le 1.0$) as 5 V Cathode Materials. *J. Power Sources* **2012**, *216*, 368−375.
(16) Kim, M. C.; Nam, K.-W.; Hu, E.; Yang, X.-Q.; Kim, H.; Kang, K.; Aravindan, V.; Kim, W.-S.; Lee, Y.-S. Sol−Gel Synthesis of Aliovalent Vanadium-Doped $LiNi_{0.5}Mn_{1.5}O_4$ Cathodes with Excellent Performance at High Temperatures. *ChemSusChem* **2014**, *7*, 829−834.
(17) Yang, Z.; Jiang, Y.; Kim, J.-H.; Wu, Y.; Li, G.-L.; Huang, Y.-H. The $LiZn_xNi_{0.5-x}Mn_{1.5}O_4$ Spinel with Improved High Voltage Stability for Li-Ion Batteries. *Electrochim. Acta* **2014**, *117*, 76−83.
(18) Yi, T.-F.; Chen, B.; Zhu, Y.-R.; Li, X.-Y.; Zhu, R.-S. Enhanced Rate Performance of Molybdenum-Doped Spinel $LiNi_{0.5}Mn_{1.5}O_4$ Cathode Materials for Lithium Ion Battery. *J. Power Sources* **2014**, *247*, 778−785.
(19) Chen, Z.; Qiu, S.; Cao, Y.; Ai, X.; Xie, K.; Hong, X.; Yang, H. Surface-Oriented and Nanoflake-Stacked $LiNi_{0.5}Mn_{1.5}O_4$ Spinel for High-Rate and Long-Cycle-Life Lithium Ion Batteries. *J. Mater. Chem.* **2012**, *22*, 17768−17772.
(20) Hai, B.; Shukla, A. K.; Duncan, H.; Chen, G. The Effect of Particle Surface Facets on the Kinetic Properties of $LiMn_{1.5}Ni_{0.5}O_4$ Cathode Materials. *J. Mater. Chem. A* **2013**, *1*, 759−769.
(21) Chemelewski, K. R.; Lee, E.-S.; Li, W.; Manthiram, A. Factors Influencing the Electrochemical Properties of High-Voltage Spinel Cathodes: Relative Impact of Morphology and Cation Ordering. *Chem. Mater.* **2013**, *25*, 2890−2897.
(22) Chemelewski, K. R.; Shin, D. W.; Li, W.; Manthiram, A. Octahedral and Truncated High-Voltage Spinel Cathodes: The Role of Morphology and Surface Planes in Electrochemical Properties. *J. Mater. Chem. A* **2013**, *1*, 3347−3354.
(23) Lin, H. B.; Zhang, Y. M.; Rong, H. B.; Mai, S. W.; Hu, J. N.; Liao, Y. H.; Xing, L. D.; Xu, M. Q.; Li, X. P.; Li, W. S. Crystallographic Facet- and Size-Controllable Synthesis of Spinel $LiNi_{0.5}Mn_{1.5}O_4$ with Excellent Cyclic Stability as Cathode of High Voltage Lithium Ion Battery. *J. Mater. Chem. A* **2014**, *2*, 11987−11995.
(24) Chen, Z.; Zhao, R.; Du, P.; Hu, H.; Wang, T.; Zhu, L.; Chen, H. Polyhedral $LiNi_{0.5}Mn_{1.5}O_4$ with Excellent Electrochemical Properties for Lithium-Ion Batteries. *J. Mater. Chem. A* **2014**, *2*, 12835−12848.
(25) Chen, Z.; Zhao, R.; Li, A.; Hu, H.; Liang, G.; Lan, W.; Cao, Z.; Chen, H. Polyhedral Ordered $LiNi_{0.5}Mn_{1.5}O_4$ Spinel with Excellent Electrochemical Properties in Extreme Conditions. *J. Power Sources* **2015**, *274*, 265−273.
(26) Liu, H.; Kloepsch, R.; Wang, J.; Winter, M.; Li, J. Truncated Octahedral $LiNi_{0.5}Mn_{1.5}O_4$ Cathode Material for Ultralong-Life Lithium-Ion Battery: Positive (100) Surfaces in High-Voltage Spinel System. *J. Power Sources* **2015**, *300*, 430−437.
(27) Liu, H.; Wang, J.; Zhang, X.; Zhou, D.; Qi, X.; Qiu, B.; Fang, J.; Kloepsch, R.; Schumacher, G.; Liu, Z.; Li, J. Morphological Evolution of High-Voltage Spinel $LiNi_{0.5}Mn_{1.5}O_4$ Cathode Materials for Lithium-Ion Batteries: The Critical Effects of Surface Orientations and Particle Size. *ACS Appl. Mater. Interfaces* **2016**, *8*, 4661−4675.
(28) Yi, T.-F.; Mei, J.; Zhu, Y.-R. Key Strategies for Enhancing the Cycling Stability and Rate Capacity of $LiNi_{0.5}Mn_{1.5}O_4$ as High-Voltage Cathode Materials for High Power Lithium-Ion Batteries. *J. Power Sources* **2016**, *316*, 85−105.
(29) Park, O. K.; Cho, Y.; Lee, S.; Yoo, H.-C.; Song, H.-K.; Cho, J. Who Will Drive Electric Vehicles, Olivine or Spinel? *Energy Environ. Sci.* **2011**, *4*, 1621−1633.
(30) Manthiram, A.; Chemelewski, K.; Lee, E.-S. A Perspective on the High-Voltage $LiMn_{1.5}Ni_{0.5}O_4$ Spinel Cathode for Lithium-Ion Batteries. *Energy Environ. Sci.* **2014**, *7*, 1339−1350.
(31) Ma, J.; Hu, P.; Cui, G.; Chen, L. Surface and Interface Issues in Spinel $LiNi_{0.5}Mn_{1.5}O_4$: Insights into a Potential Cathode Material for High Energy Density Lithium Ion Batteries. *Chem. Mater.* **2016**, *28*, 3578−3606.
(32) Li, W.; Song, B.; Manthiram, A. High-Voltage Positive Electrode Materials for Lithium-Ion Batteries. *Chem. Soc. Rev.* **2017**, *46*, 3006.
(33) Hu, M.; Pang, X.; Zhou, Z. Recent Progress in High-Voltage Lithium Ion Batteries. *J. Power Sources* **2013**, *237*, 229−242.
(34) Andre, D.; Kim, S.-J.; Lamp, P.; Lux, S. F.; Maglia, F.; Paschos, O.; Stiaszny, B. Future Generations of Cathode Materials: An Automotive Industry Perspective. *J. Mater. Chem. A* **2015**, *3*, 6709−6732.
(35) Kraytsberg, A.; Ein-Eli, Y. Higher, Stronger, Better···□ a Review of 5 V Cathode Materials for Advanced Lithium-Ion Batteries. *Adv. Energy Mater.* **2012**, *2*, 922−939.
(36) Lee, E.; Persson, K. A. First-Principles Study of the Nano-Scaling Effect on the Electrochemical Behavior in $LiNi_{0.5}Mn_{1.5}O_4$. *Nanotechnology* **2013**, *24*, 424007.
(37) Shin, D. W.; Manthiram, A. Surface-Segregated, High-Voltage Spinel $LiMn_{1.5}Ni_{0.42}Ga_{0.08}O_4$ Cathodes with Superior High-Temperature Cyclability for Lithium-Ion Batteries. *Electrochem. Commun.* **2011**, *13*, 1213−1216.
(38) Chemelewski, K. R.; Li, W.; Gutierrez, A.; Manthiram, A. High-Voltage Spinel Cathodes for Lithium-Ion Batteries: Controlling the Growth of Preferred Crystallographic Planes through Cation Doping. *J. Mater. Chem. A* **2013**, *1*, 15334−15341.
(39) Amatucci, G.; Tarascon, J.-M. Optimization of Insertion Compounds Such as $LiMn_2O_4$ for Li-Ion Batteries. *J. Electrochem. Soc.* **2002**, *149*, K31−K46.
(40) Luo, J.; Chiang, Y. M. Existence and Stability of Nanometer-Thick Disordered Films on Oxide Surfaces. *Acta Mater.* **2000**, *48*, 4501−4515.
(41) Scheithauer, M.; Grasselli, R. K.; Knözinger, H. Genesis and Structure of WO_x/ZrO_2 Solid Acid Catalysts. *Langmuir* **1998**, *14*, 3019−3029.
(42) Tae Kwon, Y.; Yong Song, K.; In Lee, W.; Jin Choi, G.; Rag Do, Y. Photocatalytic Behavior of WO_3-Loaded TiO_2 in an Oxidation Reaction. *J. Catal.* **2000**, *191*, 192−199.
(43) Qiu, B.; Zhang, M. H.; Wu, L. J.; Wang, J.; Xia, Y. G.; Qian, D. N.; Liu, H. D.; Hy, S.; Chen, Y.; An, K.; Zhu, Y. M.; Liu, Z. P.; Meng, Y. S. Gas-Solid Interfacial Modification of Oxygen Activity in Layered Oxide Cathodes for Lithium-Ion Batteries. *Nat. Commun.* **2016**, *7*, 12108.
(44) Liu, H. D.; Qian, D. N.; Verde, M. G.; Zhang, M. H.; Baggetto, L.; An, K.; Chen, Y.; Carroll, K. J.; Lau, D.; Chi, M. F.; Veith, G. M.; Meng, Y. S. Understanding the Role of NH_4F and Al_2O_3 Surface Co-Modification on Lithium-Excess Layered Oxide $Li_{1.2}Ni_{0.2}Mn_{0.6}O_2$. *ACS Appl. Mater. Interfaces* **2015**, *7*, 19189−19200.
(45) An, K.; Skorpenske, H. D.; Stoica, A. D.; Ma, D.; Wang, X. L.; Cakmak, E. First in Situ Lattice Strains Measurements under Load at Vulcan. *Metall. Mater. Trans. A* **2011**, *42*, 95−99.
(46) An, K.; Wang, X. L.; Stoica, A. D. *VDRIVE: Vulcan Data Reduction and Interactive Visualization Software*; Oak Ridge National Laboratory: Oak Ridge, TN. 2012.
(47) Toby, B. H. Expgui, a Graphical User Interface for Gsas. *J. Appl. Crystallogr.* **2001**, *34*, 210−213.

DOI: 10.1021/acsami.7b09903
ACS Appl. Mater. Interfaces 2017, 9, 36745−36754

(48) Larson, A. C.; Dreele, R. B. V. *General Structure Analysis System (GSAS)*; Los Alamos National Laboratory Report (LAUR) 86-748; Los Alamos National Laboratory: Los Alamos, NM, 2004.
(49) Zucker, R. V.; Chatain, D.; Dahmen, U.; Hagège, S.; Carter, W. C. New Software Tools for the Calculation and Display of Isolated and Attached Interfacial-Energy Minimizing Particle Shapes. *J. Mater. Sci.* **2012**, *47*, 8290−8302.
(50) Liu, J.; Manthiram, A. Understanding the Improved Electrochemical Performances of Fe-Substituted 5 V Spinel Cathode $LiMn_{1.5}Ni_{0.5}O_4$. *J. Phys. Chem. C* **2009**, *113*, 15073−15079.
(51) Terada, Y.; Yasaka, K.; Nishikawa, F.; Konishi, T.; Yoshio, M.; Nakai, I. In Situ Xafs Analysis of $Li(Mn, M)_2O_4$ (M = Cr, Co, Ni) 5 V Cathode Materials for Lithium-Ion Secondary Batteries. *J. Solid State Chem.* **2001**, *156*, 286−291.
(52) Amine, K.; Tukamoto, H.; Yasuda, H.; Fujita, Y. Preparation and Electrochemical Investigation of $LiMn_{2-X}Me_xO_4$ (Me: Ni, Fe, and X = 0.5, 1) Cathode Materials for Secondary Lithium Batteries. *J. Power Sources* **1997**, *68*, 604−608.
(53) Trease, N. M.; Seymour, I. D.; Radin, M. D.; Liu, H.; Liu, H.; Hy, S.; Chernova, N.; Parikh, P.; Devaraj, A.; Wiaderek, K. M.; Chupas, P. J.; Chapman, K. W.; Whittingham, M. S.; Meng, Y. S.; Van der Van, A.; Grey, C. P. Identifying the Distribution of Al^{3+} in $LiNi_{0.8}Co_{0.15}Al_{0.05}O_2$. *Chem. Mater.* **2016**, *28*, 8170−8180.
(54) Liu, H. D.; Huang, J. J.; Qian, D. N.; Hy, S.; Fang, C. C.; Luo, J.; Meng, Y. S. Communication-Enhancing the Electrochemical Performance of Lithium-Excess Layered Oxide $Li_{1.13}Ni_{0.3}Mn_{0.57}O_2$ Via a Facile Nanoscale Surface Modification. *J. Electrochem. Soc.* **2016**, *163*, A971−A973.
(55) Liu, H. D.; Chen, Y.; Hy, S.; An, K.; Venkatachalam, S.; Qian, D. N.; Zhang, M. H.; Meng, Y. S. Operando Lithium Dynamics in the Li-Rich Layered Oxide Cathode Material Via Neutron Diffraction. *Adv. Energy Mater.* **2016**, *6*, 1502143.
(56) Liu, H. D.; Fell, C. R.; An, K.; Cai, L.; Meng, Y. S. In-Situ Neutron Diffraction Study of the $XLi_2MnO_3 \cdot (1\text{-}X)LiMO_2$ (X = 0, 0.5; M = Ni, Mn, Co) Layered Oxide Compounds During Electrochemical Cycling. *J. Power Sources* **2013**, *240*, 772−778.
(57) Chen, Y.; Cheng, Y.; Li, J.; Feygenson, M.; Heller, W. T.; Liang, C.; An, K. Lattice-Cell Orientation Disorder in Complex Spinel Oxides. *Adv. Energy Mater.* **2017**, *7*, 1601950.
(58) Cai, L.; Liu, Z.; An, K.; Liang, C. Unraveling Structural Evolution of $LiNi_{0.5}Mn_{1.5}O_4$ by in Situ Neutron Diffraction. *J. Mater. Chem. A* **2013**, *1*, 6908−6914.
(59) Qiao, R.; Wang, Y.; Olalde-Velasco, P.; Li, H.; Hu, Y.-S.; Yang, W. Direct Evidence of Gradient Mn(II) Evolution at Charged States in $LiNi_{0.5}Mn_{1.5}O_4$ Electrodes with Capacity Fading. *J. Power Sources* **2015**, *273*, 1120−1126.
(60) Kuppan, S.; Xu, Y.; Liu, Y.; Chen, G. *Nat. Commun.* **2017**, *8*, 14309.
(61) Cantwell, P. R.; Tang, M.; Dillon, S. J.; Luo, J.; Rohrer, G. S.; Harmer, M. P. Overview No. 152: Grain Boundary Complexions. *Acta Mater.* **2014**, *62*, 1−48.
(62) Luo, J. Interfacial Engineering of Solid Electrolytes. *J. Materiomics* **2015**, *1*, 22−32.
(63) Huang, J.; Luo, J. A Facile and Generic Method to Improve Cathode Materials for Lithium-Ion Batteries Via Utilizing Nanoscale Surface Amorphous Films of Self-Regulating Thickness. *Phys. Chem. Chem. Phys.* **2014**, *16*, 7786−7798.
(64) Kayyar, A.; Qian, H. J.; Luo, J. Surface Adsorption and Disordering in $LiFePO_4$ Based Battery Cathodes. *Appl. Phys. Lett.* **2009**, *95*, 221905.
(65) Luo, J.; Chiang, Y.-M. Wetting and Prewetting on Ceramic Surfaces. *Annu. Rev. Mater. Res.* **2008**, *38*, 227−249.
(66) Kang, B.; Ceder, G. Battery Materials for Ultrafast Charging and Discharging. *Nature* **2009**, *458*, 190−193.
(67) Samiee, M.; Luo, J. A Facile Nitridation Method to Improve the Rate Capability of TiO_2 for Lithium-Ion Batteries. *J. Power Sources* **2014**, *245*, 594−598.
(68) Samiee, M.; Luo, J. Pseudocapacitive Properties of Two-Dimensional Surface Vanadia Phases Formed Spontaneously on Titania. *ACS Appl. Mater. Interfaces* **2016**, *8*, 12871−12880.
(69) Samiee, M.; Luo, J. Enhancing the Visible-Light Photocatalytic Activity of TiO_2 by Heat Treatments in Reducing Environments. *Mater. Lett.* **2013**, *98*, 205−208.
(70) Chen, X. B.; Liu, L.; Yu, P. Y.; Mao, S. S. Increasing Solar Absorption for Photocatalysis with Black Hydrogenated Titanium Dioxide Nanocrystals. *Science* **2011**, *331*, 746−750.

DOI: 10.1021/acsami.7b09903
ACS Appl. Mater. Interfaces 2017, 9, 36745−36754